



Synthesis of $Ti_{0.7}Mo_{0.3}O_2$ supported-Pt nanodendrites and their catalytic activity and stability for oxygen reduction reaction

Trung-Thanh Nguyen ^{a,1}, Van Thi Thanh Ho ^a, Chun-Jern Pan ^{a,1}, Jyong-Yue Liu ^{a,1}, Hung-Lung Chou ^{b,1}, John Rick ^{a,1}, Wei-Nien Su ^{b,*1}, Bing-Joe Hwang ^{a,c,**,1}

^a Nano Electrochemistry Laboratory, Department of Chemical Engineering, National Taiwan University of Science and Technology, Taipei 106, Taiwan

^b Graduate Institute of Applied Science and Technology, National Taiwan University of Science and Technology, Taipei 106, Taiwan

^c National Synchrotron Radiation Research Center, Hsinchu 30076, Taiwan



ARTICLE INFO

Article history:

Received 10 October 2013

Received in revised form

31 December 2013

Accepted 11 February 2014

Available online 20 February 2014

Keywords:

Oxide-supported nanocatalysts

Pt nanodendrites

Mo-doped titania

Oxygen reduction reaction

Strong metal-support interaction (SMSI)

ABSTRACT

Nanostructural clusters (NCs) of dendritic Pt on $Ti_{0.7}Mo_{0.3}O_2$ nanosupports ($Pt_d/Ti_{0.7}Mo_{0.3}O_2$ -NCs) were synthesized by a simple aqueous-phase route. $PtCl_6^{2-}$ -ions were reduced and formed nuclei under the effect of L-ascorbic acid and cetyltrimethylammonium bromide (CTAB). There followed controlled deposition and growth of Pt nanoparticles with high-index facets of Pt. In the synthesis, the clustering of the Pt particles could be driven by their high surface energy due to a large surface area-to-volume ratio. 20 wt% dendritic Pt/ $Ti_{0.7}Mo_{0.3}O_2$ -NCs and support-free Pt nanodendrite catalysts were prepared and compared against commercial 20 wt% Pt/C (E-TEK) for oxygen reduction reaction (ORR). TEM, XRD, X-ray absorption near edge structure (XANES), and electrochemical techniques were applied to characterize these catalysts. Effects of high index facets on dendritic Pt surface, electron transfer originating from strong metal-support interactions (SMSI) and corrosion-resistant $Ti_{0.7}Mo_{0.3}O_2$ nanosupport contribute to the enhanced catalytic activity and stability of Pt/ $Ti_{0.7}Mo_{0.3}O_2$ -NCs toward the ORR. The concept of the $Pt_d/Ti_{0.7}Mo_{0.3}O_2$ -NCs combining advantages of SMSI and Pt nanodendrites provides a new approach to design novel nanocatalysts for various reaction systems.

© 2014 Elsevier B.V. All rights reserved.

1. Introduction

The improvements of catalytic activity and durability toward oxygen reduction reaction (ORR) are the important issues before the commercialization of Polymer Electrolyte Membrane Fuel Cells (PEMFC) [1]. The composition, size and shape controlled Pt-based nanocrystals were attested to be suitable and efficient catalysts for these purposes [2]. Actually, these strategies have been adopted to enhance the mass activity of the Pt-based catalysts through increasing effective Pt surface area, and intrinsic activity of active sites on the catalyst surface [3].

A variety of chemical protocols have been developed to achieve functional shapes of Pt-based nanocrystals in 1-dimensional tube [4] and wire [5], or 3-dimensional cube^[2f], octahedron [2a] or

concave morphologies [3b,3f], porous [2d,6] and branched or even dendrite materials [1a,2d,7]. Among them, the dendritic morphology of Pt nanocrystals has attracted the particular interest due to their branched structure, high surface area, and high catalytic activity for ORR [8]. Furthermore, bimetallic Pt-based nanocrystals with a dendritic Pt shell showed significant improvements for ORR performance. For example, Zhang's [7] and Xia's [9] works showed the Pd@Pt nanodendrites exhibited higher catalytic activity and stability for ORR than commercial Pt/C. Additionally, the morphology of Au nanocore affects the catalytic activity and durability of Au@Pt nanodendrites and their ORR performance is higher than that of monometallic Pt nanodendrite [1a]. The enhancement of activity of these binary Pt-M catalysts is attributed to the electronic donation of the second transition metal (M) to Pt surface, which modifies the electronic structure of Pt surface atoms that results in a weakened interaction between Pt and intermediates, freeing more active sites for O_2 adsorption [1e,10].

Additionally, corrosion of the carbon supports at high potentials becomes prominent and the phenomenon causes reduced stability and performance of the carbon supported-Pt catalyst in fuel cell systems [11]. To avoid the consequences of eroded carbon support, researchers have suggested the use of metal oxide supports.

* Corresponding author. Tel.: +886 2 27333141; fax: +886 2 27376922.

** Corresponding author. Fax: +886 2 27376644.

E-mail addresses: wsu@mail.ntust.edu.tw, weinien.su@gmail.com (W.-N. Su), bjh@mail.ntust.edu.tw (B.-J. Hwang).

¹ Current address: National Taiwan University of Science and Technology, Taipei 106, Taiwan.

Chemically inert TiO₂-based materials are frequently chosen out of the economic reason and properties, such as Ti_{0.7}W_{0.3}O₂, Nb-doped TiO₂, RuO₂–TiO₂ and Ti₄O₇ oxides [12]. A series of anatase-Ti_xM_{1-x}O₂ (M=Mo [13], Ru [14]) nanosupports were explored in our previous works where Ti_{0.7}Mo_{0.3}O₂ played as a functionalized co-catalytic support for Pt nanoparticles toward ORR. These nanosupports not only solve the above carbon-corrosion issues but also enhance the catalytic activity for ORR, due to strong metal–support interaction (SMSI) between the metal oxide and the Pt catalyst, resulting in modifying the electronic nature of the metal particles [13,14].

These efforts indicate that both Pt morphology and the composition and structural features of the support can significantly affect catalytic activity and stability for the ORR. However, the deposition of Pt with controlled morphology has not been well-explored yet. High index facets of Pt surfaces have not been observed on these oxide-supported Pt catalyst due to small sizes. It is hoped to achieve a higher ORR catalytic activity and stability, by combining the advantages of dendritic Pt and Ti_xM_{1-x}O₂. Herein, Pt dendrites were synthesized on Ti_{0.7}Mo_{0.3}O₂ nanosupports in the presence of L-ascorbic acid (AA) and Cetyl Trimethylammonium Bromide (CTAB) as a reductant agent and surfactant, respectively. The synergy of nanostructural clusters (NCs) of Ti_{0.7}Mo_{0.3}O₂-supported Pt nanodendrites (Pt_d/Ti_{0.7}Mo_{0.3}O₂-NCs) is discussed with various characterization methods. Commercial Pt/C and support-free Pt nanodendrites were also included in the study to compare their electrochemical activity and stability.

2. Experimental

2.1. Chemicals and materials

Titanium chloride (TiCl₄, ACROS), molybdenum(V) chloride (MoCl₅, Aldrich), dihydrogen hexachloroplatinate(IV) hexahydrate (H₂PtCl₆·6H₂O, 99.9%, 38–40% Pt, ACROS); L-ascorbic acid (AA, Sigma-Aldrich); cetyltrimethylammonium bromide (CTAB, ACROS); sulfuric acid (ACROS, 98%). Deionized water (DI water) was used in all experiments.

2.2. Synthesis of Ti_{0.7}Mo_{0.3}O₂ nanoparticles and Pt_d/Ti_{0.7}Mo_{0.3}O₂ nanodendrite

2.2.1. Synthesis of Ti_{0.7}Mo_{0.3}O₂ nanoparticles

Ti_{0.7}Mo_{0.3}O₂ nanoparticles were prepared by employing a hydrothermal method with low temperature and free-stabilizer (or free-surfactant) as described in our previous work [13]. In a typical synthesis, 50 mL of a precursor solution, including 12 mM MoCl₅ ad 28 mM TiCl₄ (with Mo:Ti = 3:7 molar ratio), was transferred to a Teflon-lined autoclave with a stainless steel shell. Next, the system was heated and kept at 200 °C for 2 h in an oven. After the heating, the system was cooled down to room temperature. Ti_{0.7}Mo_{0.3}O₂ was washed with DI water and collected by centrifugation several times until the washings showed pH 7. The precipitates were dried at 80 °C in a vacuum oven overnight (>8 h) for the electrochemical and textural analyses.

2.2.2. Synthesis of Pt_d/Ti_{0.7}Mo_{0.3}O₂-NCs

To synthesize 20 wt% Pt_d/Ti_{0.7}Mo_{0.3}O₂-NCs, Ti_{0.7}Mo_{0.3}O₂ nanoparticles were introduced as nano-substrates for the growth of Pt nanodendrites (with multi-branches). Herein, a wet method was employed in the presence of AA as special reductant and CTAB as the surfactant to produce a dense array of Pt dendrites. In a typical synthesis, 20 mL of the suspension solution, containing 0.08 g of nanoparticles, 0.05 g of CTAB and 0.04 g of AA, was ultrasonically dispersed. The reactor was sealed and then heated to 80 °C in an oil bath with a hot plate and strong stirring (400 rpm).

After keeping a steady state of heating at 80 °C for 20 min, 5 mL of Pt precursor solution (H₂PtCl₆; with Pt:Ti_{0.7}Mo_{0.3}O₂ = 1:4 weight ratio) was injected into the suspension solution by dropping with a micropipette at a rate of 10 µL per fixed time interval. It is essential that the temperature of the solution should be maintained constant (at 80 °C) during the reaction time. After the complete addition of the Pt precursor solution, the reactor was sealed and continuously heated for 3 h. Next, the system was cooled down to room temperature. The 20 wt% Pt_d/Ti_{0.7}Mo_{0.3}O₂-NCs were washed with acetone and DI water and collected by centrifugation several times to remove excessive CTAB. The precipitates were dried at 80 °C in a vacuum oven overnight (>8 h) for the electrochemical and textural analyses.

2.3. Structural characterizations

Wide Angle X-ray diffraction (WAXRD) patterns were recorded on dry glass after the aqueous dispersions of the based-Pt nanocrystals, using a D2 Phaser XRD 300 W diffractometer with a step size of 0.05°, a 30 s step time, and using Cu K α radiation ($\lambda = 1.5406 \text{ \AA}$). The morphology and particle sizes of Ti_{0.7}Mo_{0.3}O₂ and Pt_d/Ti_{0.7}Mo_{0.3}O₂-NCs were evaluated by transmission electron microscopy (TEM) on a Philips Tecnai G² F20 TEM microscope operated at 40 kV. Notably, specimens were prepared by ultrasonically suspending the nanoparticles in ethanol; the suspension was then applied to a copper grid and dried in an oven. Additionally, both of the average composition of Ti_{0.7}Mo_{0.3}O₂ support and the Pt loading of Pt_d/Ti_{0.7}Mo_{0.3}O₂ catalyst were determined by energy-dispersive X-ray spectroscopy (EDX) at 200 kV. However, the Brunauer–Emmett–Teller (BET) surface area and pore size of Ti_{0.7}Mo_{0.3}O₂ support were determined from N₂ adsorption/desorption isotherms at 77 K (Porous Materials, BET-202A). Before BET measurement, the support needed to be degassed at 300 °C for 24 hrs to remove completely the water molecules inside the meso-/micro-pores of this oxide. Accordingly, the BET data shown here correspond to the annealed samples. The electrical conductivity of the Ti_{0.7}Mo_{0.3}O₂ powder was measured by a standard four-probe technique (KeithLink Technology, Taiwan). Ti_{0.7}Mo_{0.3}O₂ powder was made into pellets, of ~13 mm diameter and ~1 mm thickness, by use of a steel die in a hydraulic press under a pressure of 300 MPa. To obtain reliable electrical conductivity data, the four-point probe system was carefully placed on the Ti_{0.7}Mo_{0.3}O₂ pellet, at three different sites on each sample.

X-ray adsorption spectra (XAS) were recorded at the National Synchrotron Radiation Research Centre (NSRRC) of Taiwan, beamline 01 C, following the procedure described in detail elsewhere [1c,15]. In the typical procedure of instrument specifications, cell configuration, and sample treatment for proper measurement were same as before. Measurements were made at room temperature with solid samples. Pt foil was used as references for Pt L_{III}-edge measurements. The control of parameters for extended X-ray absorption fine structure (EXAFS) measurements, data collection modes, and calculation of errors were all done as per the guidelines set by the International XAFS Society Standards and Criteria Committee [1c,15].

2.4. Pt loading examination

The Pt loading on support was determined both by of energy-dispersive X-ray spectroscopic (EDX-JSM 6500F, JEOL) with an accelerating voltage of 15 kV and inductively coupled plasma-atomic emission spectrometry (ICP-AES). The average composition of the support material, and catalyst nanocatalysts were also obtained using an EDX-JSM 6500F, JEOL with an accelerating voltage of 10 kV.

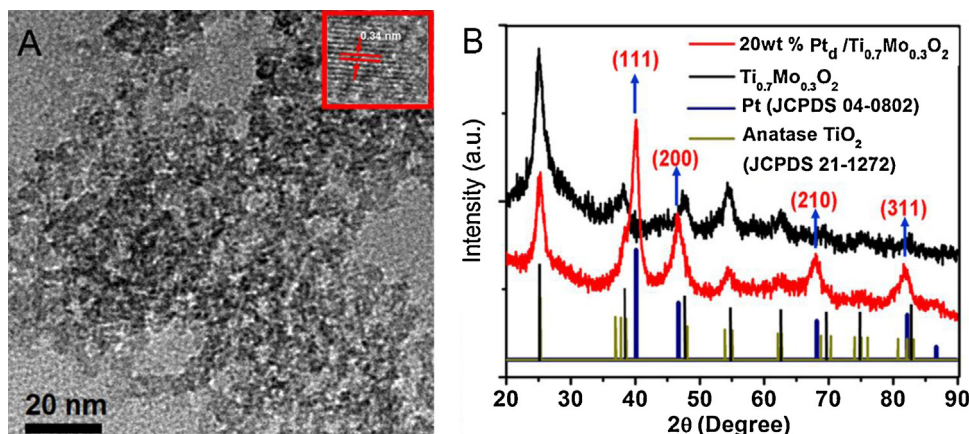


Fig. 1. (A) TEM and (inset) HR-TEM images of $\text{Ti}_{0.7}\text{Mo}_{0.3}\text{O}_2$ material and (B) X-ray diffraction patterns of $\text{Ti}_{0.7}\text{Mo}_{0.3}\text{O}_2$ nanosupport and 20 wt% $\text{Pt}_d/\text{Ti}_{0.7}\text{Mo}_{0.3}\text{O}_2$ -NC catalyst.

2.5. Electrode preparation and electrochemical measurements

Analytical grade Millipore water ($18\text{ M}\Omega$) and sulfuric acid were used in this study. All of the experiments were carried out at ambient temperature of $25 \pm 1^\circ\text{C}$, unless stated otherwise. A conventional three-electrode electrochemical cell, connected to a Solartron 1480 potentiostat/galvanostat, was used for the electrochemical measurement, with a high surface area Pt counter electrode and the saturated calomel electrode (SCE) as a reference electrode. All potentials in this article were quoted with respect to the reversible hydrogen electrode (RHE). A thin layer of Nafion-impregnated $\text{Pt}_d/\text{Ti}_{0.7}\text{Mo}_{0.3}\text{O}_2$ catalyst cast on a glassy carbon disk (PINE) of 5 mm diameter (0.196 cm^2 area) embedded in a Teflon holder was dispersed in 0.5% Nafion by sonication for 3 h, and $7\text{ }\mu\text{L}$ of catalyst suspension containing 6.2 mg of Pt mL^{-1} was placed on the glassy carbon electrode (GCE) surface and dried at 80°C for 15 min to produce a uniform thin film of the catalyst. The 0.5 M sulfuric acid was used as supporting electrolyte for all of the experiments.

3. Results and discussion

3.1. Characterization of $\text{Ti}_{0.7}\text{Mo}_{0.3}\text{O}_2$ support material

Black $\text{Ti}_{0.7}\text{Mo}_{0.3}\text{O}_2$ powder was prepared by mixing TiCl_4 and MoCl_5 precursors in aqueous solution under a simple hydrothermal method at 200°C . More details can be referred to the experimental section in the supporting information (SI). The features of $\text{Ti}_{0.7}\text{Mo}_{0.3}\text{O}_2$ powder were characterized by Transition Electron Microscopy (TEM), X-ray diffraction (XRD), Resonance Raman spectroscopy and Brunauer–Emmett–Teller (BET) surface area measurements. The results are shown in Fig. 1 and Figure S1 (in the SI). The features of as-prepared $\text{Ti}_{0.7}\text{Mo}_{0.3}\text{O}_2$ nanoparticles can be summarized as a single solid-solution with anatase TiO_2 structure, high surface area of $224.8\text{ m}^2\text{ g}^{-1}$ and electronic conductivity of $2.8 \times 10^{-4}\text{ S cm}^{-1}$ over anatase- TiO_2 nanoparticles. The size distribution of $\text{Ti}_{0.7}\text{Mo}_{0.3}\text{O}_2$ nanoparticles lies between 8 and 10 nm.

3.2. Characterization of $\text{Pt}_d/\text{Ti}_{0.7}\text{Mo}_{0.3}\text{O}_2$ catalysts and the formation mechanism of dendritic Pt layer on $\text{Ti}_{0.7}\text{Mo}_{0.3}\text{O}_2$ nanosupports

The XRD patterns of 20 wt% $\text{Pt}_d/\text{Ti}_{0.7}\text{Mo}_{0.3}\text{O}_2$ NCs are displayed in Fig. 1B. The XRD data exhibited that the structure of Pt nanodendrites on $\text{Ti}_{0.7}\text{Mo}_{0.3}\text{O}_2$ match well with those expected for face-centered cubic (FCC) Pt crystals (by using JCPDS 04-0802). The peaks located at 40.1° , 46.6° , 68.0° , 81.6° are attributed to (111),

(200), (210) and (311) planes of Pt crystals, respectively. These four peaks of diffracted Pt metal partially overlap on the diffraction peaks of $\text{Ti}_{0.7}\text{Mo}_{0.3}\text{O}_2$ material at the same positions. In addition, the broadening of peaks is consistent with the nanoscale structural features of the Pt dendrite [8]. TEM and high resolution TEM (HR-TEM) images of the as-prepared $\text{Pt}_d/\text{Ti}_{0.7}\text{Mo}_{0.3}\text{O}_2$ -NC are shown in Fig. 2A and B, where hetero-structural dendritic clusters of Pt nanocrystals supported on $\text{Ti}_{0.7}\text{Mo}_{0.3}\text{O}_2$ can be clearly observed. The NCs were formed by employing an aqueous-solution route in 80°C under ambient pressure (see the experimental section in SI). Each arm of the dendrites was ended with a rounded 2–3 nm tip (Fig. 2B). In addition, space among the arms was observed and introduced by the remaining surfactant on the rinsed Pt surfaces. The formation of dendritic Pt nanocrystals has been attributed to the reductant AA and its chelation with PtCl_6^{2-} precursor in aqueous micellar solutions [8]. However, Wang et al. recently concluded that 2,3-diketo-1-gulonic acid, which is a byproduct from AA oxidation, served as a shape-directing agent to direct the branched growth [16]. Consequently, the dendrite morphology of Pt nanocrystals can be obtained under the direct effect of AA or the byproduct from its oxidation. However, the observed non-uniform morphology and size of these clusters can be attributed to the attachment of small Pt particles on $\text{Ti}_{0.7}\text{Mo}_{0.3}\text{O}_2$ nanosupport in the cluster formation. As known, the dendritic nature of the nanostructures is more evident in the high-angle annular dark field (HAADF) scanning TEM images [17]. As shown in Figure S2A (in the SI), the morphology of the $\text{Pt}_d/\text{Ti}_{0.7}\text{Mo}_{0.3}\text{O}_2$ -NCs is non-spherical, slightly different to support-free Pt nanodendrites as in Figure S3 (in the SI) and the previous reports [7,8,17]. TEM-elemental mapping measurements in Figure S2B, C, D and E in the SI, show the detected elemental distribution of Ti, Mo, O, and Pt. In addition, the energy-dispersive X-ray spectroscopy (EDX) spectrum was also applied to confirm that clusters of 20 wt% Pt were grown on $\text{Ti}_{0.7}\text{Mo}_{0.3}\text{O}_2$ nanosupports whose Ti:Mo ratio was around 7:3, as seen in Figure S2F in the SI. ICP measurement showed real Pt loading of $\text{Pt}_d/\text{Ti}_{0.7}\text{Mo}_{0.3}\text{O}_2$ -NCs was 21.8 wt%. Additional evidence by X-ray absorption measurement will be discussed in the following text.

The HR-TEM image in Fig. 3A of the $\text{Pt}_d/\text{Ti}_{0.7}\text{Mo}_{0.3}\text{O}_2$ nanodendrite cluster indicates that Pt single crystal is present and its surface being enclosed by (111) facets. The (111) planes are commonly observed for systems containing Pt nanocrystals grown on an oxide support [13,14,18]. However, HR-TEM image of support-free Pt nanodendrites indicates that the single crystalline Pt nanodendrites were enclosed by (100) planes, as seen in Fig. 3B. It results from the fact that Br^- ions from CTAB compound preferentially adsorbs onto the Pt(100) planes [19]. It implies that the presence of oxide surface can promote the crystallization of Pt nanoparticles

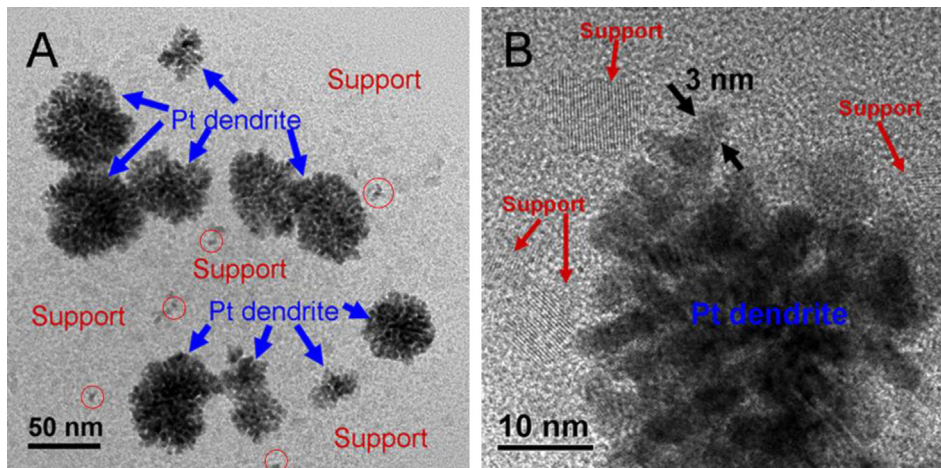


Fig. 2. (A, B) TEM images of 20 wt% $\text{Pt}_d/\text{Ti}_{0.7}\text{Mo}_{0.3}\text{O}_2$ nanodendritic-clusters. Pt bumps on $\text{Ti}_{0.7}\text{Mo}_{0.3}\text{O}_2$ nanosupports are circled in (A).

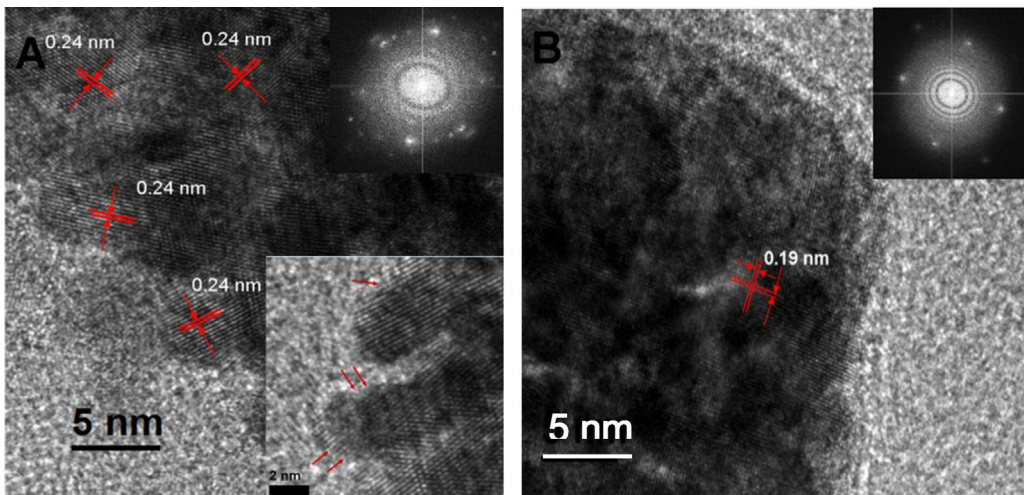


Fig. 3. HR-TEM images of $\text{Pt}_d/\text{Ti}_{0.7}\text{Mo}_{0.3}\text{O}_2$ (A) and support-free Pt nanodendrite (B), with inserts of corresponding FFT images.

in selected planes. Additional HR-TEM images of smaller $\text{Pt}_d/\text{Ti}_{0.7}\text{Mo}_{0.3}\text{O}_2$ -NCs are given in Figure S4 as evidences for the formation of nanostructured $\text{Pt}_d/\text{Ti}_{0.7}\text{Mo}_{0.3}\text{O}_2$. The lattice fringes of Pt were also found not aligned across the entire dendritic structure, as the result of successive growth of dendritic structure.

The growth mechanism can be understood and proposed as follows. Pt nanocrystals started from the seeding on the $\text{Ti}_{0.7}\text{Mo}_{0.3}\text{O}_2$ and a bump-like hetero-nanostructure initially (circled in Fig. 2A) formed from the metastable solution due to lattice mismatch between two different materials. Next, $\text{Pt}/\text{Ti}_{0.7}\text{Mo}_{0.3}\text{O}_2$ hetero-nanostructure grew and clustered from the original Pt bumps on $\text{Ti}_{0.7}\text{Mo}_{0.3}\text{O}_2$ nanocrystals into Pt dendrites. The growth of Pt(1 1 1) bumps on $\text{Ti}_{0.7}\text{Mo}_{0.3}\text{O}_2$ was largely driven by their high energy due to a large surface area-to-volume ratio. Different Pt bumps on $\text{Ti}_{0.7}\text{Mo}_{0.3}\text{O}_2$ were also attached and assembled into larger clustered structure, where Pt bumps played a role of “connectors”. Finally, complete $\text{Pt}_d/\text{Ti}_{0.7}\text{Mo}_{0.3}\text{O}_2$ -NCs were formed by successive growth of Pt dendrites onto the $\text{Pt}/\text{Ti}_{0.7}\text{Mo}_{0.3}\text{O}_2$ nanoclusters as Pt precursor solution was injected into the solution in a controlled manner. The morphology and size of original $\text{Pt}/\text{Ti}_{0.7}\text{Mo}_{0.3}\text{O}_2$ nanoclusters would greatly depend on the processing conditions and details. It is noted that the high index facets are also observed on the Pt branches as shown in the insert image of Fig. 3A. The whole mechanism is proposed and illustrated in Scheme 1.

X-ray absorption spectroscopy (XAS) measurements were performed on the $\text{Pt}_d/\text{Ti}_{0.7}\text{Mo}_{0.3}\text{O}_2$, support-free Pt nanodendrites, and Pt/C (E-Tek, 20 wt % Pt nanoparticles on Vulcan XC-72 carbon support, TEM image of E-Tek as shown in Figure S5) and the spectra are shown in Fig. 4. The absorption peak, namely white lines, of dendrite $\text{Pt}_d/\text{Ti}_{0.7}\text{Mo}_{0.3}\text{O}_2$ -NCs at the L_{III} edge was lower

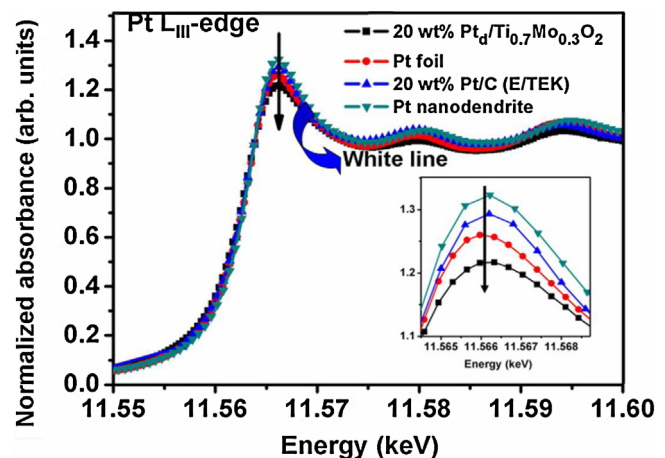
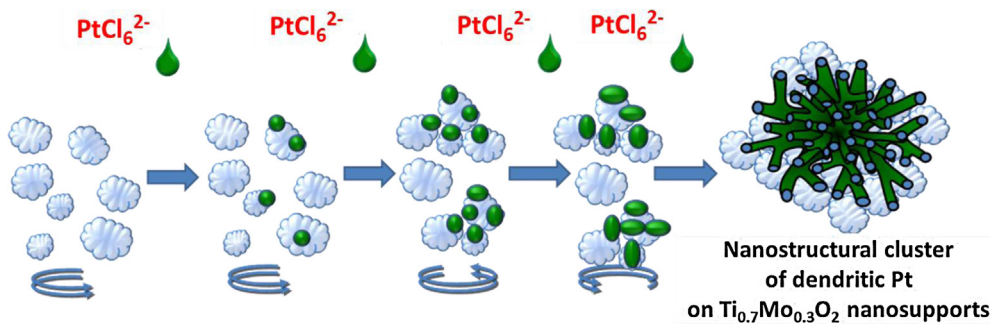


Fig. 4. Pt L_{III} -edge XANES spectra and Pt foil used as reference.



Scheme 1. Hetero-nanoclusters of dendrite $\text{Pt}_d/\text{Ti}_{0.7}\text{Mo}_{0.3}\text{O}_2$ obtained under appropriate dosing intervals of Pt^{4+} and the functions of CTAB and AA.

than the corresponding peaks for support-free Pt nanodendrites, and Pt/C (E-Tek) and Pt foil, indicating decreased d-band vacancy which was attributed to the electron donation from $\text{Ti}_{0.7}\text{Mo}_{0.3}\text{O}_2$ nanosupport to Pt caused by the strong metal support interactions (SMSI). On the contrary, support-free Pt nanodendrites showed an increase d-band vacancy because of the electronic interaction with the attached N-centered surfactant molecules and nanosize effect.

3.3. Electrochemical performances of Pt catalysts

The electrocatalytic activity of the 20 wt% $\text{Pt}_d/\text{Ti}_{0.7}\text{Mo}_{0.3}\text{O}_2$ -NCs toward the ORR were investigated and compared against support-free Pt nanodendrites and a commercial sample (Pt/C, E-Tek) as the references. A rotating disk electrode (RDE) with a constant cross-section area is 0.196 cm^2 , was employed for all performances of the electrochemical measurement. Hydrogen adsorption and desorption is a powerful technique to determine the electrochemical surface area (ECSA) of a Pt electrode [20], and a sweep rate of 25 mV s^{-1} was chosen for the experiments of the hydrogen adsorption and desorption processes for all catalysts. It is to note that the experiments were conducted with the same loading of Pt ($0.221\text{ mg Pt cm}^{-2}$) on a glassy carbon electrode (GCE) as a standardized condition. The cyclic voltammetry (CV) curves of these catalysts were recorded at room temperature (25°C) in N_2 -purged $0.5\text{ M H}_2\text{SO}_4$ solutions, as seen in Fig. 5A (see experimental part for details). The CV curves exhibited potential regions associated with H_{upd} adsorption and desorption processes ($\text{H}^+ + \text{e}^- = \text{H}_{\text{upd}}$) from 0 to 0.4 V and reversible adsorption of OH_{ad} ($2\text{H}_2\text{O} = \text{OH}_{\text{ad}} + \text{H}_3\text{O}^+ + \text{e}^-$) beyond 0.6 V , where H_{upd} and OH_{ad} refer to the under-potentially deposited hydrogen and the adsorbed hydroxyl species, respectively [21]. By means of hydrogen adsorption/desorption methods and with the CV, the ECSA of each catalyst could be calculated in the standard region from 0.02 V to 0.4 V , after double-layer correction, assuming a value of $210\text{ }\mu\text{C/cm}^2$ for the adsorption of a hydrogen monolayer. The specific values of ECSA based on the Pt mass for $\text{Pt}_d/\text{Ti}_{0.7}\text{Mo}_{0.3}\text{O}_2$, Pt nanodendrite and Pt/C (E-Tek) were found to be 81.07 , 71.54 and $71.17\text{ m}^2\text{ g}_{\text{Pt}}^{-1}$, respectively. The highest ECSA of $\text{Pt}_d/\text{Ti}_{0.7}\text{Mo}_{0.3}\text{O}_2$ catalyst indicates that this deposition of Pt nanodendrites on the $\text{Ti}_{0.7}\text{Mo}_{0.3}\text{O}_2$ nanosupports exhibits a higher active surface area despite its larger overall particle size. It can be attributed to the structural difference of Pt surface [22]. No oxidation or reduction peak was observed for molybdenum oxide from $\text{Pt}_d/\text{Ti}_{0.7}\text{Mo}_{0.3}\text{O}_2$ in Fig. 5A, implying that this support material is highly stable in acidic solutions and oxidative environment.

Catalytic activity with respect to the ORR was determined in O_2 -saturated aqueous H_2SO_4 (0.5 M) solutions using a glassy carbon RDE at 25°C at a sweep rate of 1 mV s^{-1} and a rotation rate of 1600 rpm . The polarization curves for the catalysts are shown in Fig. 5B. The current densities were normalized to the geometric surface area of the glassy carbon electrode (0.196 cm^2). As shown

in Fig. 5B, a number of important conclusions can be drawn by looking at the differences in the onset potential, half wave potential and limiting current values [23]. The onset potential is more positive on $\text{Pt}_d/\text{Ti}_{0.7}\text{Mo}_{0.3}\text{O}_2$ electrode and faster ORR is observed in the high potential range than that on dendritic Pt and Pt/C electrodes. When compared with other electrodes, the half wave potential of $\text{Pt}_d/\text{Ti}_{0.7}\text{Mo}_{0.3}\text{O}_2$ electrode also shifts to higher potential. The limiting current densities on three types of electrodes are almost the same. The resemblance in the diffusion-controlled current is explained by the similar oxygen diffusion in these electrodes. All these features for the electrode of $\text{Pt}_d/\text{Ti}_{0.7}\text{Mo}_{0.3}\text{O}_2$ will contribute to an improved ORR activity, which is discussed in latter paragraphs.

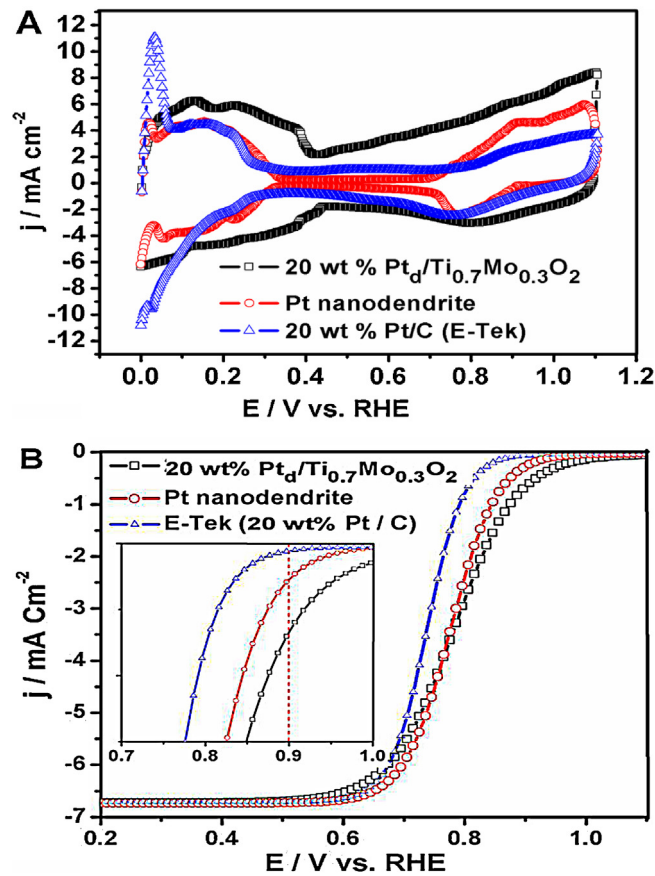


Fig. 5. (A) Cyclic voltammogram curves (at the scanning rate of 25 mV s^{-1}); (B) Polarization curves showing the ORR current (at the scanning rate of 1 mV s^{-1}) of 20 wt% $\text{Pt}_d/\text{Ti}_{0.7}\text{Mo}_{0.3}\text{O}_2$; Pt nanodendrite and 20 wt% Pt/C (E-Tek) catalysts in N_2 -saturated $0.5\text{ M H}_2\text{SO}_4$ solutions.

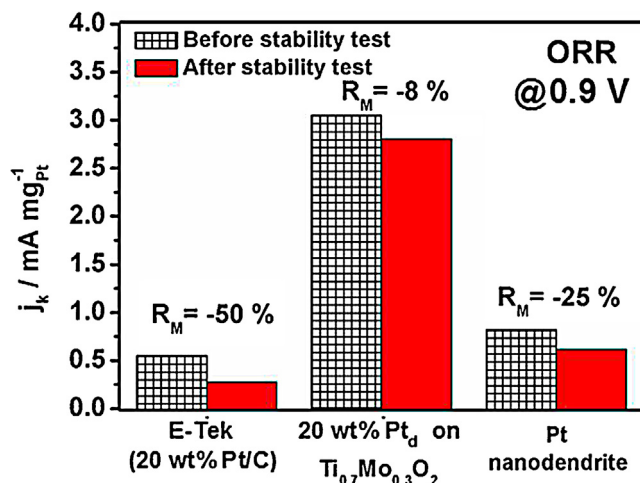


Fig. 6. Stability characterization and mass activity of 20 wt% Pt_d/Ti_{0.7}Mo_{0.3}O₂; dendritic Pt and 20 wt% Pt/C (E-Tek) catalysts (R_M : reduction percentages of mass activity).

For a better understanding of different ORR activities, the kinetic current (j_k) associated with the intrinsic activity of the catalysts was obtained using a Koutecky-Levich equation for oxygen reduction with different catalysts [24]. In order to compare the Pt mass activities for Pt-based catalysts the kinetic current was calculated from the polarization curve by applying a mass transport correction and then normalizing with respect to the loading amount of Pt (Fig. 6). The experimental results demonstrate that, at 0.9 V, the Pt mass activities of the catalysts for the ORR depend on the structure of materials. It is worth mentioning that both home-made materials (namely support-free Pt nanodendrite and Pt_d/Ti_{0.7}Mo_{0.3}O₂-NCs) exhibited excellent catalytic activities and higher than that of the commercial Pt catalyst (Pt/C, E-Tek). Especially, the Pt_d/Ti_{0.7}Mo_{0.3}O₂ nanocrystal has the highest catalyst activity for ORR and was found to be ~5.5 times and ~3.7 times as active as commercial 20 wt% Pt/C (E-Tek) and support-free Pt nanodendrite with an equivalent Pt mass. Thus, the order of catalytic activity is Pt_d/Ti_{0.7}Mo_{0.3}O₂ > Pt nanodendrite > Pt_{nano}particles/C. As shown, both of the home-made dendritic Pt nanocrystals outperformed the commercial catalyst in catalyzing of the ORR, which can be attributed to the advantages conferred by the high index facets of dendritic structure over conventional Pt nanocrystals. The adsorption of O₂ molecules is more favorable onto the stepped surfaces [25]. Additionally, the highly catalytic activity of Pt_d/Ti_{0.7}Mo_{0.3}O₂ over support-free Pt nanodendrites can be explained by the contribution of Ti_{0.7}Mo_{0.3}O₂ support, such as high surface area and electronic transfer mechanism from Ti_{0.7}Mo_{0.3}O₂ support to metallic Pt nanodendrites, leading to a shift in the d-band center of the surface Pt atoms. The bimetal oxide, besides being a robust support material for Pt, also participates strongly in bonding, including d-orbital bond strain, leading to a reduced intermediate adsorptive strength for Pt in the rate-determining step. Thus, more active sites for O₂ adsorption are available to facilitate a faster reaction. (The contributions of individual shells of atoms are separated visually for Pt nanocatalysts are displayed in Figure S6.)

The stability tests consisted of repetitive cycles by applying potential steps between 0.2 and 1.2 V (versus RHE) in O₂-saturated H₂SO₄ (0.5 M) electrolyte at 25 °C. The reduction percentages of mass activity (R_M) for all catalysts were then determined by comparing the mass activity before and after stability tests as shown in Fig. 6 and Table S1. The complete polarization curves before and after stability tests can be found in Figure S7 (in SI). The Pt_d/Ti_{0.7}Mo_{0.3}O₂ catalyst not only showed good catalytic activity,

but also exhibited excellent catalytic stability because it exhibited the lowest R_M (~8%). This can be ascribed to the advantages of Ti_{0.7}Mo_{0.3}O₂ such as very stable in acidic environment and strong interaction between Pt and Ti_{0.7}Mo_{0.3}O₂. However, Pt/C (E-Tek) shows a poor stability, because carbon can be eroded by the oxidation at high potentials and the interaction between Pt metal and carbon support is much weaker. In fact, the size of Pt nanodendrites is larger than that commercial Pt/C catalyst, whereby it gives a better stability against corrosion [2d].

4. Conclusions

A simple protocol for the synthesis of Pt_d/Ti_{0.7}Mo_{0.3}O₂ was developed using AA and CTAB as a reductant and surfactant via an aqueous route. It was found that the hetero-nanostructural clusters of Pt_d/Ti_{0.7}Mo_{0.3}O₂ were grown by the gradual attachment of small Pt particles on Ti_{0.7}Mo_{0.3}O₂ nanosupports. The growth mechanism Pt dendrites could be mainly driven by their high surface energy due to a large surface area-to-volume ratio of Pt nanoparticles. In the electrochemical measurements, Pt_d/Ti_{0.7}Mo_{0.3}O₂ showed a significant enhancement in catalytic activity and durability for the ORR over the support-free Pt nanodendrites and commercial Pt nanoparticles on carbon support (E-Tek). The improvements can be attributed to the synergy of the SMSI from Ti_{0.7}Mo_{0.3}O₂ nanosupport and dendritic Pt nanocrystals which have more high-index facets exposed. As the issue of carbonaceous support corrosion is getting more attention, the adoption of oxide support has been seen as one of the options to mitigate the problem. We hope that the developed synthesis protocol could be an enlightened approach for the further development of oxide-supported catalysts for various applications, such as ORR, hydrogenation, and CO oxidation.

Supporting information available

XRD patterns, BET curves, TEM images and results of electrochemical measurements can be found in the supporting information.

Acknowledgments

We are grateful for financial support from the National Science Council (NSC 102-ET-E-011-002-ET, NSC 102-3113-P-011-001) and the "Top Universities Project" (100H451401) from the Ministry of Education (MoE). We also thank to the Department of Chemical Engineering, National Taiwan University of Science and Technology (NTUST) for providing research facilities.

Appendix A. Supplementary data

Supplementary data associated with this article can be found, in the online version, at <http://dx.doi.org/10.1016/j.apcatb.2014.02.018>.

References

- [1] (a) Y. Kim, J.W. Hong, Y.W. Lee, M. Kim, D. Kim, W.S. Yun, S.W. Han, *Angewandte Chemie International Edition* 49 (2010) 10197–10201;
 (b) W.-P. Zhou, X. Yang, M.B. Vukmirovic, B.E. Koel, J. Jiao, G. Peng, M. Mavrikakis, R.R. Adzic, *Journal of the American Chemical Society* 131 (2009) 12755;
 (c) F.-J. Lai, L.S. Sarma, H.-L. Chou, D.-G. Liu, C.-A. Hsieh, J.-F. Lee, B.-J. Hwang, *The Journal of Physical Chemistry C* 113 (2009) 12674–12681;
 (d) C. Wang, H. Daimon, S. Sun, *Nano Letters* 9 (2009) 1493–1496;
 (e) S.-H. Chang, W.-N. Su, M.-H. Yeh, C.-J. Pan, K.-L. Yu, D.-G. Liu, J.-F. Lee, B.-J. Hwang, *Chemistry: A European Journal* 16 (2010) 11064–11071;
 (f) F. Taufany, C.-J. Pan, J. Rick, H.-L. Chou, M.-C. Tsai, B.-J. Hwang, D.-G. Liu, J.-F. Lee, M.-T. Tang, Y.-C. Lee, C.-I. Chen, *ACS Nano* 5 (2011) 9370–9381;
 (g) S.W. Lee, S. Chen, J. Suntivich, K. Sasaki, R.R. Adzic, Y. Shao-Horn, *The Journal of Physical Chemistry Letters* 1 (2010) 1316–1320.

- [2] (a) J. Wu, A. Gross, H. Yang, *Nano Letters* 11 (2011) 798–802;
 (b) B.J. Hwang, S.M.S. Kumar, C.-H. Chen, Monalisa, M.-Y. Cheng, D.-G. Liu, J.-F. Lee, *The Journal of Physical Chemistry C* 111 (2007) 15267;
 (c) C. Venkateswara Rao, B. Viswanathan, *The Journal of Physical Chemistry C* 113 (2009) 18907;
 (d) C. Kim, J.-G. Oh, Y.-T. Kim, H. Kim, H. Lee, *Electrochemistry Communications* 12 (2010) 1596–1599;
 (e) K. Yamamoto, T. Imaoka, W.-J. Chun, O. Enoki, H. Katoh, M. Takenaga, A. Sonoi, *Nature Chemistry* 1 (2009) 397–402;
 (f) C. Wang, H. Daimon, Y. Lee, J. Kim, S. Sun, *Journal of the American Chemical Society* 129 (2007) 6974–6975.
- [3] (a) H.A. Gasteiger, S.S. Kocha, B. Sompalli, F.T. Wagner, *Applied Catalysis B: Environmental* 56 (2005) 9–35;
 (b) H. Zhang, M. Jin, J. Wang, W. Li, P.H.C. Camargo, M.J. Kim, D. Yang, Z. Xie, Y. Xia, *Journal of the American Chemical Society* 133 (2011) 6078–6089;
 (c) J. Greeley, I.E.L. Stephens, A.S. Bondarenko, T.P. Johansson, H.A. Hansen, T.F. Jarillo, Rossmeisl, J.K. Chorkendorff, Nørskov, *Nature Chemistry* 1 (2009) 552–556;
 (d) F.-J. Lai, W.-N. Su, L.S. Sarma, D.-G. Liu, C.-A. Hsieh, J.-F. Lee, B.-J. Hwang, *Chemistry: A European Journal* 16 (2010) 4602–4611;
 (e) N. Tian, Z.-Y. Zhou, S.-G. Sun, *The Journal of Physical Chemistry C* 112 (2008) 19801;
 (f) T. Yu, D.Y. Kim, H. Zhang, Y. Xia, *Angewandte Chemie International Edition* 50 (2011) 2773–2777.
- [4] Z. Chen, M. Waje, W. Li, Y. Yan, *Angewandte Chemie International Edition* 46 (2007) 4060.
- [5] (a) E.P. Lee, J. Chen, Y. Yin, C.T. Campbell, Y. Xia, *Advanced Materials* 18 (2006) 3271;
 (b) E.P. Lee, Z. Peng, D.M. Cate, H. Yang, C.T. Campbell, Y. Xia, *Journal of the American Chemical Society* 129 (2007) 10634.
- [6] S.M. Alia, G. Zhang, D. Kisailus, D. Li, S. Gu, K. Jensen, Y. Yan, *Advanced Functional Materials* 20 (2010) 3742.
- [7] H. Zhang, Y. Yin, Y. Hu, C. Li, P. Wu, S. Wei, C. Cai, *The Journal of Physical Chemistry C* 114 (2010) 11861–11867.
- [8] Y. Song, Y.-B. Jiang, D.A. Pena, Y. Qiu, J.E. Miller, J.A. Shelnutt, *Nanotechnology* 17 (2006) 1300.
- [9] B. Lim, M. Jiang, P.H.C. Camargo, E.C. Cho, J. Tao, X. Lu, Y. Zhu, Y. Xia, *Science* 324 (2009) 1302–1305.
- [10] R. Adzic, J. Zhang, K. Sasaki, M. Vukmirovic, M. Shao, J. Wang, A. Nilekar, M. Mavrikakis, J. Valerio, F. Uribe, *Topics in Catalysis* 46 (2007) 249–262, <http://link.springer.com/article/10.1007/s11244-007-9003-x>.
- [11] (a) M.S. Wilson, J.A. Valerio, S. Gottesfeld, *Electrochimica Acta* 40 (1995) 355;
 (b) G.S. Kumar, M. Raja, S. Parthasarathy, *Electrochimica Acta* 40 (1995) 285.
- [12] (a) D. Wang, C.V. Subban, H. Wang, E. Rus, F.J. DiSalvo, H.D. Abruna, *Journal of the American Chemical Society* 132 (2010) 10218;
 (b) K.-W. Park, K.-S. Seol, *Electrochemistry Communications* 9 (2007) 2256;
 (c) A. Wang, H. Xu, Y. Lu, J. Hu, X. Kong, B. Tian, H. Dong, *Chinese Journal of Catalysis* 30 (2009) 179;
 (d) T. Ioroi, Z. Siroma, N. Fujiwara, S.-I. Yamazaki, K. Yasuda, *Electrochemistry Communications* 7 (2005) 183.
- [13] V.T.T. Ho, C.-J. Pan, J. Rick, W.-N. Su, B.-J. Hwang, *Journal of the American Chemical Society* 133 (2011) 11716.
- [14] V.T.T. Ho, K.C. Pillai, H.-L. Chou, C.-J. Pan, J. Rick, W.-N. Su, B.-J. Hwang, J.-F. Lee, H.-S. Sheu, W.-T. Chuang, *Energy & Environmental Science* 4 (2011) 4194.
- [15] B.J. Hwang, S.M.S. Kumar, C.-H. Chen, R.-W. Chang, D.-G. Liu, J.-F. Lee, *The Journal of Physical Chemistry C* 112 (2008) 2370.
- [16] L. Wang, Y. Nemoto, Y. Yamauchi, *Journal of the American Chemical Society* 133 (2011) 9674–9677.
- [17] Y. Song, Y. Yang, C.J. Medforth, E. Pereira, A.K. Singh, H. Xu, Y. Jiang, C.J. Brinker, F. van Swol, J.A. Shelnutt, *Journal of the American Chemical Society* 126 (2003) 635.
- [18] (a) X. Gong, Y. Yang, S. Huang, *Chemical Communications* 47 (2011) 1009;
 (b) Y.L. Shen, C.S. Song, J.M. Song, T.K. Chin, C.H. Lin, I.G. Chen, *Nanoscale Research Letters* 6 (2011) 380;
 (c) J.N. Tiwari, R.N. Tiwari, K.-L. Lin, *ACS Applied Materials & Interfaces* 2 (2010) 2231.
- [19] A.-X. Yin, X.-Q. Min, Y.-W. Zhang, C.-H. Yan, *Journal of the American Chemical Society* 133 (2011) 3816–3819.
- [20] J.N. Tiwari, R.N. Tiwari, K.-L. Lin, *ACS Applied Materials & Interfaces* 2 (2010) 2231–2237.
- [21] R. Gómez, J.M. Orts, B. Álvarez-Ruiz, J.M. Feliu, *The Journal of Physical Chemistry B* 108 (2003) 228–238.
- [22] N.V. Long, T. Duy Hien, T. Asaka, M. Ohtaki, M. Nogami, *International Journal of Hydrogen Energy* 36 (2011) 8478.
- [23] R. Vellacheri, S.M. Unni, S. Nahire, U.K. Kharul, S. Kurungot, *Electrochimica Acta* 55 (2010) 2878.
- [24] A.J. Bard, L.R. Faulkner in Vol. *Electrochemical Methods: Fundamentals and Applications*, 2nd Edition, Wiley, New York, 2000, ISBN: 978-0-471-04372-0, (<http://as.wiley.com/WileyCDA/WileyTitle/productCd-0471043729.html>).
- [25] (a) D.W. Blakely, G.A. Somorjai, *Surface Science letters* 65 (1997) 419;
 (b) N.M. Marković, R.R. Adžić, B.D. Cahan, E.B. Yeager, *Journal of Electroanalytical Chemistry* 377 (1994) 249.